

# Comparison of the detector response and calibration function of metallic microcalorimeters for X-ray photons and external electrons

Neven Kovač<sup>a,\*</sup>, Fabienne Adam<sup>a,b,\*</sup>, Sebastian Kempf<sup>b,c</sup>, Marie-Christin Langer<sup>b</sup>, Michael Müller<sup>b</sup>, Rudolf Sack<sup>a</sup>, Magnus Schlösser<sup>a</sup>, Markus Steidl<sup>a</sup>, Kathrin Valerius<sup>a</sup>

<sup>a</sup>*Institute for Astroparticle Physics (IAP) - Karlsruhe Institute of Technology (KIT), Hermann-von-Helmholtz-Platz 1, 76344, Eggenstein-Leopoldshafen, Germany*

<sup>b</sup>*Institute of Micro- and Nanoelectronic Systems (IMS) - Karlsruhe Institute of Technology (KIT), Hertzstraße 16, 76187, Karlsruhe, Germany*

<sup>c</sup>*Institute for Data Processing and Electronics (IPE) - Karlsruhe Institute of Technology (KIT), Hermann-von-Helmholtz-Platz 1, 76344, Eggenstein-Leopoldshafen, Germany*

---

## Abstract

Metallic microcalorimeters (MMCs) are cryogenic single-particle detectors that rely on a calorimetric detection principle. Due to their excellent energy resolution, close-to-ideal linear detector response, fast signal rise time and the potential for 100 % quantum efficiency, MMCs outperform conventional detectors by several orders of magnitude in resolution. These attributes make them particularly interesting for a broad spectrum of applications, including a next-generation neutrino mass experiment based on the measurement of the tritium beta-decay spectrum, with an objective of achieving a sensitivity surpassing that of the pioneering KATRIN experiment. However, although MMCs have been used in measurements of photons and heavy ions with great success, no information is currently available on the interaction between MMCs and external light charged particles such as electrons. This work aims to provide such missing information and to demonstrate that MMC-based detectors are suitable for high-resolution spectroscopy of external electron sources. Particularly, we present the first-ever measurements of external electrons using a metallic microcalorimeter, comprehensively discuss the characteristics of the signal shape and the calibration function and

---

\*Corresponding authors

give a direct comparison between well-defined conversion electron and X-ray photon signals from the same  $^{83}\text{Rb}/^{83m}\text{Kr}$  source.

*Keywords:* Metallic Microcalorimeters, Quantum Sensors, Neutrino Mass, Electron Spectroscopy, Krypton-83m, Tritium

---

## 1. Introduction

The discovery of neutrino oscillations at the end of last millennium provided compelling evidence that neutrinos are massive particles [1, 2]. Due to their copious production in the early Universe, neutrinos played a key role in structure formation, as well as in the evolution and expansion of the Universe [3]. However, oscillation experiments cannot provide any information on the absolute scale of the neutrino mass and a different, direct approach is required. Today, the measurement of the absolute scale of the neutrino mass in a model-independent way is one of the most important and pressing questions in contemporary physics.

The only model-independent experimental approach is based on kinematic analysis of weak decay processes, most notably the  $\beta$  decay of tritium [4]. Here, the effect of non-zero neutrino mass manifests itself as a distortion and a shift of the end-point region of the measured electron energy spectrum from the tritium decay [5].

Currently, by far the most constraining limits on the neutrino mass obtained from direct measurements come from the KATRIN (**K**ARlsruhe **T**RITium **N**eutrino) experiment hosted at the Tritium Laboratory Karlsruhe (TLK) [6]. The KATRIN experiment consists of a 70 m long beamline, designed to probe the electron anti-neutrino mass by high-resolution and high-statistics measurements of the electron spectrum, produced in the beta-decay of a gaseous molecular tritium source. The working principle of the KATRIN experiment is based on the MAC-E (Magnetic Adiabatic Collimation with Electrostatic) filter technology [7, 8, 9], which analyses the energy of individual electrons by acting as a high-pass energy filter. By counting the number of electrons that pass the filter at each predefined retardation energy using a multi-pixel silicon *p-i-n*-diode array, an integral spectrum can be reconstructed. Recently, an upper limit on the electron anti-neutrino mass was determined to be  $m_{\bar{\nu}_e} \leq 0.45 \text{ eV}/c^2$  at 90% CL [10]. The final sensitivity of the KATRIN experiment is about 0.3 eV [6], after 1000 days of measurement, and is expected to be reached at the end of 2025.

The current technology employed by KATRIN does not allow for significant scaling to reach beyond the final sensitivity. Therefore, future neutrino-mass experiments necessitate the development of next-generation technology in order to reach the inverted mass regime, and possibly below that. To this end, KATRIN++ has been proposed as a next-generation neutrino-mass experiment, with the goal to identify and develop new scalable technology by making use of the existing infrastructure of KATRIN. Two primary concepts have been identified as key for the success of the future experiment: (1) an ultra-high-resolution differential detection method and (2) a high luminosity atomic tritium source.

Currently, KATRIN uses a molecular tritium source in which spectral broadening originating from molecular final states limits the effective resolution of the measurement to about 1 eV FWHM. In a future experiment an atomic source needs to be employed in order to mitigate this limitation.

Furthermore, switching from an integral measurement mode, currently employed at KATRIN, to a differential one, will allow for a much more efficient collection of statistics, a substantial reduction of background and an increase in the energy resolution of the experiment. New detector technology will need to be able to resolve the energy of individual electrons, with an energy resolution (FWHM) better than 1 eV. One option for such detectors are cryogenic quantum sensors such as metallic microcalorimeters (MMCs) which, at the time of writing of this article, provide a record energy resolution of  $\Delta E_{\text{FWHM}} = 1.25 \text{ eV}$  for 5.9 keV soft and tender X-ray photons [11, 12], with future prospects of reaching sub-eV energy resolution. This fact makes MMCs a highly appealing candidate for a detector in a future neutrino mass experiment using tritium. MMCs have already been employed for example in the framework of the ECHo experiment aiming to determine the electron neutrino mass by performing a calorimetric measurement of the electron capture spectrum of an implanted  $^{163}\text{Ho}$  source [13]. However, so far MMCs have never been used for measurements of electrons emitted by an external source, to the best of our knowledge. For this reason, systematic effects on the energy resolution due to the interaction between an MMC and external electrons such as backscattering, sputtering and creation of Frenkel pairs need to be experimentally studied and very well understood. In the work at hand, we present the first ever measurements of external electrons using a metallic microcalorimeter. We comprehensively discuss the characteristics of the signal shape and the calibration function and give a direct comparison to the signals from X-ray photons.

## 2. Magnetic Microcalorimeters (MMCs)

Magnetic microcalorimeters (MMCs) are cryogenic single-particle detectors that rely on a calorimetric detection principle [14, 15]. They consist, as schematically shown in figure 1, of an application-specific particle absorber and a paramagnetic temperature sensor that are strongly coupled to each other. Moreover, the absorber is weakly coupled to a heat bath with temperature  $T < 50$  mK, allowing the detector to thermalize at a well-defined baseline temperature in the absence of an energy input. The temperature sensor is biased by a weak external magnetic field of a few mT to induce a temperature-dependent sensor magnetization. In this configuration, a temperature change resulting from an energy deposition in the absorber causes a decrease in the magnetization of the paramagnetic sensor, which can be measured with highest precision by means of a superconducting flux transformer. The latter is formed by a superconducting pick-up coil magnetically coupled to the temperature sensor as well as the input coil of a current-sensing direct-current superconducting quantum interference device (dc-SQUID).

To fully stop the impinging particle, the absorber has to be made out of a material featuring a high stopping power for the particle type to be detected. Gold has been the dominant material choice for photon detection due to it being a radiopure noble metal, that is easy to deposit by microfabrication techniques, and has no metastable states. In addition, gold possesses a good thermal conductivity and a high atomic number, which is favorable since the absorption of photons occurs primarily via the photoelectric effect [15]. The downside of gold is its comparably large heat capacity, which spoils the energy resolution. For this reason, alternative absorber materials are investigated. As paramagnetic sensor material, gold or silver doped with a few hundred ppm of the rare earth metal erbium has established as the state of the art over the last decades [16, 14].

Various detector geometries exist for realizing an MMC [14, 15]. The current design of choice is based on a planar, superconducting meander-shaped pick-up coil [14, 17]. Here, as schematically depicted in figure 1, the overall pick-up coil consists of two planar meander-shaped coils that are gradiometrically connected to the input coil of the current-sensing dc-SQUID. On top of each coil, a temperature sensor and a particle absorber are placed. In addition to detecting the magnetization change within the paramagnetic temperature sensor, the meander-shaped coils are used to generate the bias magnetic field by carrying a persistent current. Due to the gradiometric

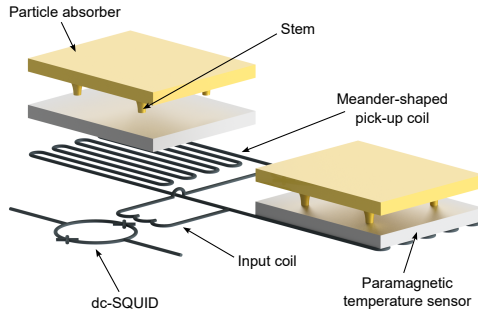


Figure 1: Schematic sketch of the state of the art detector geometry with two meander-shaped pick-up coils connected in parallel to the input coil of a current-sensing dc-SQUID. Absorber and planar temperature sensor are connected to each other via stems, which reduce energy loss to the substrate due to athermal phonon escape.

geometry of the pick-up coils, the magnetic field will have same magnitude but different sign, leading to opposite polarization of the two sensors. In this way, the signals from the two pixels will have different polarity, too, allowing them to be distinguished from each other.

### 3. Measurement Set-up

All measurements presented in this paper were performed in a commercial dilution refrigerator with a base temperature below 7 mK. We used a custom detector set-up made out of copper to guarantee a reliable thermalization of the detectors. Figure 2 shows a close-up of the setup that mainly consists of a massive copper bar, a detector platform, a  $^{83}\text{Rb}/^{83\text{m}}\text{Kr}$  source, and a hollow aluminum cylinder that is mounted on a copper carrier plate and serves as superconducting shielding. The detector platform consists of a massive copper plate that is equipped with two independent detector chips, each featuring four individual, two-pixel MMCs based on the meander-shaped geometry shown in figure 1. The overall setup hence comprises eight pixels in total. The detector chips were originally fabricated in the framework of the PrimA-LTD project [18] and were optimized for measuring the electron capture spectrum of  $^{55}\text{Fe}$ . Hence, each  $175\ \mu\text{m} \times 175\ \mu\text{m}$ -sized gold absorber measures  $12\ \mu\text{m}$  in thickness. Each MMC channel is read-out by one custom current-sensing dc-SQUID located on a separate first-stage SQUID chip placed directly next to the detector chip to minimize parasitic inductances induced by the wiring between the chips. For the measurement, the detec-

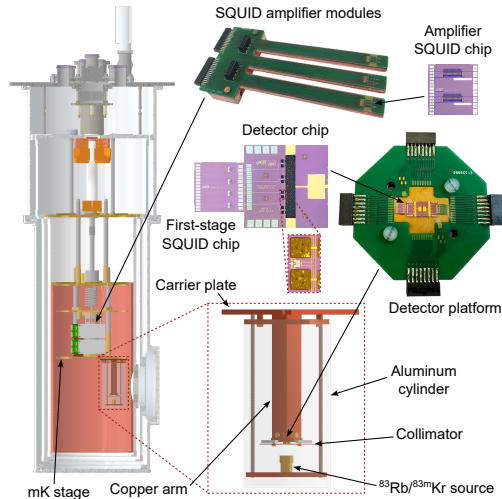


Figure 2: Schematic of the cryogenic measurement setup. A detailed description of all components is given in Section 3.

tor platform is covered by a microfabricated gold collimator with openings slightly smaller than the size of the particle absorbers to prevent charging effects by electrons hitting the substrate. The detector platform is mounted at the end of a 12.5 cm long copper bar close to the bottom of the surrounding aluminum cylinder. Inside the aluminum cylinder, a  $^{83}\text{Rb}/^{83\text{m}}\text{Kr}$  source is mounted facing the detector platform. It is attached to the same copper plate carrying the massive copper bar hosting the detector platform but with two separate threaded rods to minimize thermal contact between the source and the detector. The electron source is based on the meta-stable  $^{83\text{m}}\text{Kr}$  isomer which is produced in the decay of  $^{83}\text{Rb}$  with a branching ratio of 74(5) % and a half-life of 86.2(1) days [19]. The  $^{83}\text{Rb}$  atoms are implanted into a highly-oriented pyrolytic graphite substrate (HOPG) at the Bonn Isotope Separator (BONIS) [20]. With a half-life of 1.8 hours,  $^{83\text{m}}\text{Kr}$  decays via a cascade of two gamma transitions of 9 keV and 32.2 keV energy which are highly converted [21]. Therefore, the resulting spectrum consists of multiple mono-energetic conversion electron lines in the range between 7.5 keV and 32.1 keV as well as several X-ray lines, the most notable ones being the  $K_\alpha$  line at 12.6 keV and the  $K_\beta$  line at 14.1 keV [21].

The first-stage dc-SQUIDs reading out the MMCs were connected to custom  $N$ -dc-SQUID series arrays acting as an amplifier stage and boosting the first-stage dc-SQUID signals. Each dc-SQUID series array was connected to

commercially available room temperature electronics. The amplifier SQUIDs were assembled in custom SQUID array modules that are surrounded by superconducting as well as soft-magnetic shielding. These modules are separately attached to the mK stage of the cryostat to avoid heat dissipation in the vicinity of the detector module.

## 4. Results

In order to characterize the response of MMCs to external electrons, we measured the  $^{83\text{m}}\text{Kr}$  decay spectrum with an average event rate per pixel of about 0.1 Bq. As  $^{83\text{m}}\text{Kr}$  provides both conversion electrons and X-ray photons, direct comparison of the detector response upon photon and electron impact can be obtained with a single measurement. We acquired  $\geq 100$  traces for each selected  $^{83\text{m}}\text{Kr}$  line and averaged the recorded signals for each line. Averaging improves the signal-to-noise ratio (SNR), allowing the detector response to be more easily compared and, in particular, to see potential spurious effects. In addition, we removed traces which deviate noticeably in shape and size with a  $\chi^2$  cut.

We selected the following  $^{83\text{m}}\text{Kr}$  spectral lines for the analysis: higher energy  $L_{32-2,3}$  and  $K_{32}$  conversion electron lines,  $K_{\alpha-1}$  and  $K_{\beta-1,3}$  X-ray lines and lower energy  $M_{9-1}$  and  $L_{9-1}$  conversion electron lines. The number of selected traces as well as the energy of each selected line are reported in table 1. Figure 3 shows the averaged signal traces in linear and semi-logarithmic representation as well as a zoom into the signal rise. Overall, the agreement between the shape of the different averaged signal traces is excellent and indicates that there is no systematic deviation between signals resulting from electrons and from photons.

### 4.1. Shape of the Detector Signal

For an ideal microcalorimeter that can be modeled by a canonical ensemble with two sub-systems representing the absorber and the thermometer, each signal trace can be described by the sum of two exponentials representing the signal rise and decay [15]. However, as the finite system bandwidth of the SQUID read-out introduces a cutoff frequency  $f_r$  (usually in the range of 1 MHz), the detector response function used to describe the signal induced flux change  $\Delta\Phi$  in the first-stage SQUID needs to be modified, taking the form [22]:

Line	Particle type	Energy (keV)	# Traces
$L_{32-2,3}$	$e^-$	30.4516	363
$K_{32}$	$e^-$	17.8242	142
$K_{\beta-1,3}$	$\gamma$	14.1102	1177
$K_{\alpha-1}$	$\gamma$	12.648	5487
$K_{\alpha-2}$	$\gamma$	12.595	3719
$M_9-1$	$e^-$	9.1129	105
$L_9-1$	$e^-$	7.4811	524

Table 1: Energy and number of averaged traces for the  $^{83\text{m}}\text{Kr}$  lines selected for the analysis. The energy values of the respective lines are taken from [21].  $K_{\alpha-2}$  line is not used in the analysis, and the information is only included here for completeness.

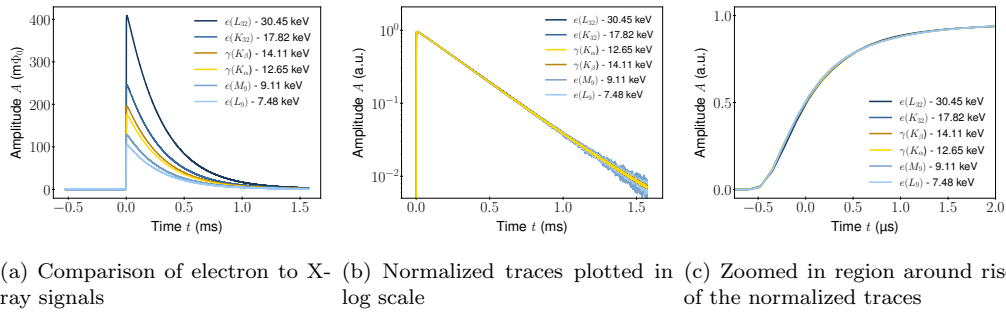


Figure 3: MMC detector response to the energy input from photons (shades of yellow) and electrons (shades of blue) emitted by the  $^{83}\text{Rb}/^{83\text{m}}\text{Kr}$  source. We selected in total six  $^{83\text{m}}\text{Kr}$  spectral lines for the analysis: two from X-ray photons and four from conversion electrons. The plots show (a) averaged signal traces, (b) normalized averaged signal traces in logarithmic scale and (c) normalized averaged signals, zoomed in the region around the signal rise.

$$\Delta\Phi(t) = A \cdot \left\{ \frac{\tau_1}{\tau_1 - \tau_r} (e^{-t/\tau_1} - e^{-t/\tau_r}) - \frac{\tau_0}{\tau_0 - \tau_r} (e^{-t/\tau_0} - e^{-t/\tau_r}) \right\}. \quad (1)$$

Here,  $A$  is the amplitude of the pulse,  $\tau_0$  is the signal rise time constant,  $\tau_1$  is the signal decay (thermalization) time constant and  $\tau_r$  is the characteristic



time constant given by  $\tau_r = 1/(2\pi f_r)$ , with  $f_r$  being the cutoff frequency of the readout system. In addition, depending on the complexity of the detector design, the detector response might show not a single but several decay constants, with one dominant exponential function which can be attributed to the thermalization of the detector with the heat bath via weak thermal link.

In order to compare the detector response to external electrons and X-ray photons, each signal trace shown in figure 3 is fitted with the function from equation 1. Figure 4 (a) displays an example of such a fit. Prior to fitting, each trace is scaled to a unitary amplitude. The fit region is limited to  $t \in [0, 0.5]$  ms, as in this region the contribution from additional exponential functions in the decay part is negligible. Figure 4 (b) shows the comparison of the fit results for the signal rise time (yellow) and signal decay time (blue). The decay time constant weakly increases with increasing energy of the particle, which can be attributed to a small change in the heat capacity and thermal conductance associated with a larger temperature increase for larger energy inputs. For similar reasons, the rise time shows a slight temperature dependence. Overall, the agreement between obtained fit parameters is consistent with expectations, and does not show a dependence on the particle type.

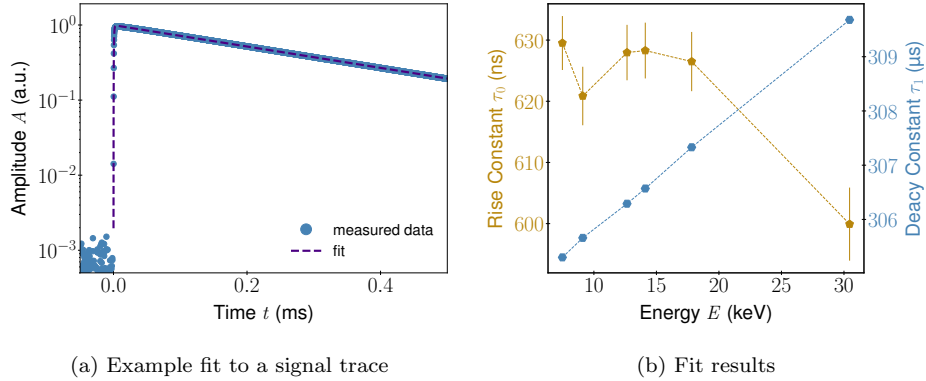


Figure 4: (a) Example fit to a single trace using the fit function from equation 1. (b) Rise time constant  $\tau_0$  and decay time constant  $\tau_1$  versus line peak energy as determined from fitting equation 1 to the different average signals shown in figure 3. Note: Uncertainties on the determined decay times constants are too small to be visible in the plot.

#### 4.2. Pulse Shape Consistency

An important check that the detector responds to photons and external electrons in the same way is to compare the difference between signal response for both particle types. In the data acquisition software used for the presented measurement, each signal trace is acquired with a time window of about 2 ms, split into 16384 discrete samples. If the pulse shapes associated with different signals are consistent, a histogram constructed from the calculated differences between two pulses is expected to be Gaussian distributed, with the width depending on detector noise.

Figure 5 shows three such plots, each with three histograms showing the trace difference between two X-ray signals (blue), two electron signals (green) and finally the difference between an electron and an X-ray signal (yellow). Signals that were chosen for the comparison are those closest to one another in energy. Figure 5 (a) shows the difference if only the 0.1 ms region around the signal rise part is considered, figure 5 (b) shows the same difference but now taking into account the signal part within 0.5 ms around the signal rise, and finally, figure 5 (c) shows the histograms if 1.0 ms around the signal rise is used. All the histograms show the expected Gaussian shape, which was confirmed by performing a Gaussian fit to the distributions, giving a mean  $\mu$  consistent with 0 for all nine histograms. Standard deviation  $\sigma$  for electron-gamma histograms (yellow) and gamma-gamma histograms (blue) is on the order of  $10^{-3}$ , while electron-electron histograms (green) feature a slightly larger  $\sigma$  of  $1.5 \times 10^{-3}$ , which can be attributed to a smaller amplitude of the signals and therefore worse SNR. Values of the fit parameters are reported in table 2, together with the reduced- $\chi^2$  of the respective fits. In addition, no visible structures appeared in the residuals, as shown in Appendix A. This detailed analysis shows that pulse shape is consistent and independent of the particle type and the energy within a given energy window.

#### 4.3. Calibration Function

Another important piece of information is whether the non-linearity and the calibration function differ for external electron and X-ray photons. For MMCs, as for other cryogenic detectors, a slight non-linearity is expected, i.e., the measured energy is not linearly related to the energy of the incoming particle. This is due to the fact that the thermodynamic properties of the detector depend on temperature and slightly change with the energy of the incoming particle [14]. To estimate the non-linearity, we fit a polynomial function to the measured amplitudes of the six selected  $^{83\text{m}}\text{Kr}$  peaks

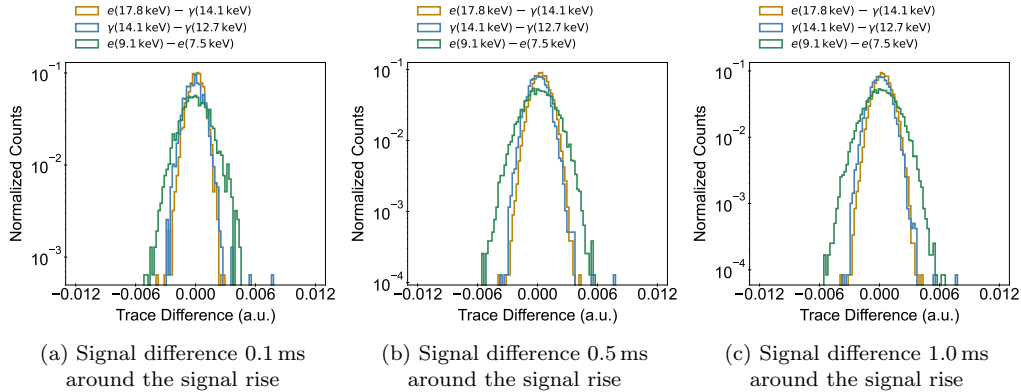


Figure 5: Histograms of the differences between individual signal traces: electron versus electron signal, photon versus photon signal and electron versus photon signal. Signals were chosen such that they are closest to one another in energy, and all histograms are normalized to 1. Individual panels correspond to the trace difference (a) in the region of 0.1 ms around the signal rise, (b) in the region of 0.5 ms around the signal rise, and (c) in the region of 1.0 ms around the signal rise.

and use the information on the true energy of the peaks, taken from [21]. To estimate the amplitude of individual peaks, each peak is fitted with an appropriate function; all electron peaks are fitted with a skewed Gaussian function which takes into account the effect of backscattering of electrons on the absorber of the detector. On the other side, the  $K_\alpha$  peak is fitted with a double Gaussian function due to the proximity of the  $K_{\alpha-1}$  and  $K_{\alpha-2}$  peaks (as reported in table 1), and the  $K_{\beta-1,3}$  peak is fitted with a single Gaussian function<sup>1</sup>. The peak amplitude is then given by the position(s) of the maxima of the respective fitted Gaussians. Figure 6 shows the measured histograms of the different peaks as well as the applied fit functions. The corresponding line positions are reported in the legend together with their respective uncertainty.

Using the obtained peak amplitudes together with the known energy of individual spectral lines, the calibration function can be obtained from a polynomial fit. The fit was performed with both second and third order polynomial functions, both of which are shown in figure 7 (a). The use of second or third order polynomial functions is justified by the fact that for larger en-

---

<sup>1</sup> $K_{\beta-1}$  and  $K_{\beta-3}$  are only separated by 8 eV, and cannot be differentiated with the current detector resolution.

Signal difference	Time window around signal rise	$\mu$	$\sigma$	$\chi^2 / \text{ndf}$
$e^- - \gamma$	0.1 ms	0.000 038	0.000 794	1.16
$\gamma - \gamma$	0.1 ms	-0.000 139	0.000 958	1.06
$e^- - e^-$	0.1 ms	-0.000 036	0.001 486	1.21
$e^- - \gamma$	0.5 ms	0.000 379	0.000 925	1.01
$\gamma - \gamma$	0.5 ms	0.000 056	0.000 957	1.38
$e^- - e^-$	0.5 ms	0.000 192	0.001 563	1.27
$e^- - \gamma$	1.0 ms	0.000 357	0.000 891	1.32
$\gamma - \gamma$	1.0 ms	0.000 076	0.000 958	1.38
$e^- - e^-$	1.0 ms	0.000 21	0.001 547	1.16

Table 2: Fit parameters,  $\mu$  and  $\sigma$ , from the Gaussian fit to the histograms of trace differences, shown in figure 5. Reduced- $\chi^2$  of the individual fits is also reported in the table and the residuals are shown in Appendix A.

ergy inputs, thermodynamical properties of the detector have to be taken into account [14].

In figure 7 (b), the difference between these polynomial fits and the linear behavior is shown, from which we obtain a non-linearity of only about 5% within the entire 30 keV range. Additionally, figure 7 (c) shows the residuals for both fit cases, all of which are within the  $3\sigma$ -uncertainty on the peak position. We can conclude that the second order polynomial fit is sufficient and all of the peaks, both from electron and from photon signal, are described with the same calibration function. The determined non-linearity of the detector<sup>2</sup>, being around 5% at 30 keV, is well within the expected range for a detector of such kind and design [14, 18].

## 5. Conclusion and Outlook

The main motivation of this work was to demonstrate that MMC detectors can be employed for the detection and spectroscopy of external light charged particles, i.e., electrons. The possibility to perform such measure-

<sup>2</sup>From figure 7 (b): at 30 keV, amplitude deviation from linear behavior is 1.544 keV, giving a non-linearity of 5.15%

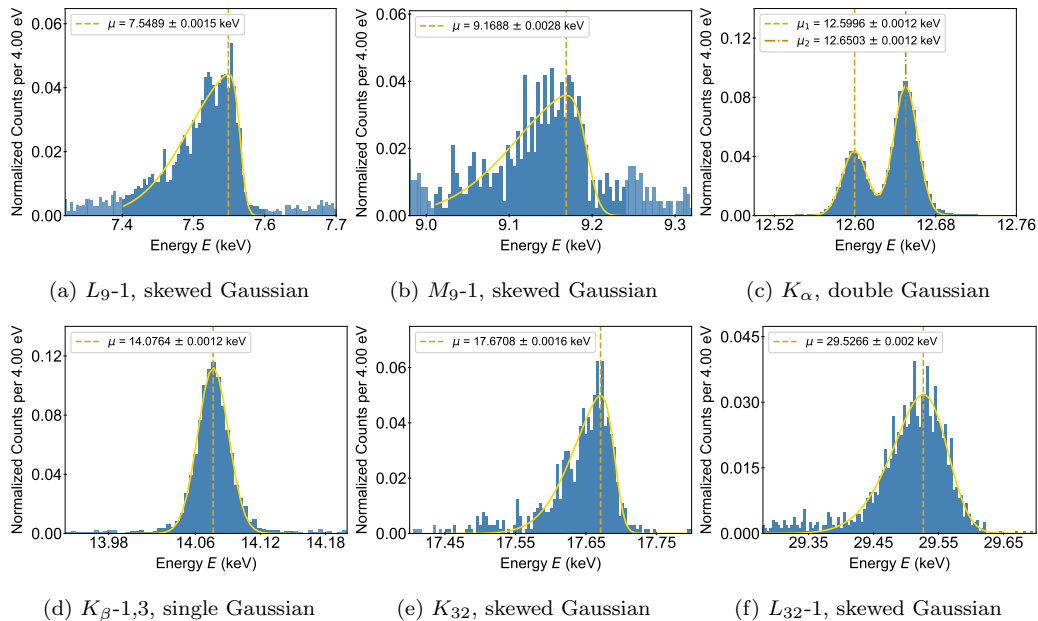


Figure 6: Fits to selected spectral lines of the  $^{83\text{m}}\text{Kr}$  spectrum: (a) fit to the  $L_{9-1}$  conversion electron peak with a skewed Gaussian, (b) fit to  $M_{9-1}$  conversion electron peak with a skewed Gaussian, (c) fit to the  $K_{\alpha}$  X-ray peak with a double Gaussian function, (d) fit to the  $K_{\beta-1,3}$  X-ray peak with a single Gaussian function, (e) fit to the  $K_{32}$  conversion electron peak with a skewed Gaussian and (f) fit to the  $L_{32-1}$  conversion electron peak with a skewed Gaussian. Obtained peak positions  $\mu$  with their uncertainties are reported in the legend.

ments would allow MMCs to be used in the field of high-resolution electron spectroscopy. Such detectors could form an enabling technology for next-generation neutrino-mass experiments, aiming to probe sub-100 meV region of the neutrino mass and ultimately go beyond the inverted mass ordering regime. The results presented in this work stand, to the best of our knowledge, as the first ever confirmation of feasibility to perform such MMC measurements, and demonstrate that there is no apparent difference in the detector response to energy deposits from external electrons versus X-ray photons. This implies that in the analysis signals from photons and external electrons do not need to be treated separately and the same analysis strategy developed over the course of previous years can be directly transferred from one use case to the other. Similar measurements have recently been conducted with Transition Edge Sensors (TESs), confirming the feasibility to use these detectors for high resolution electron spectroscopy as well [23].

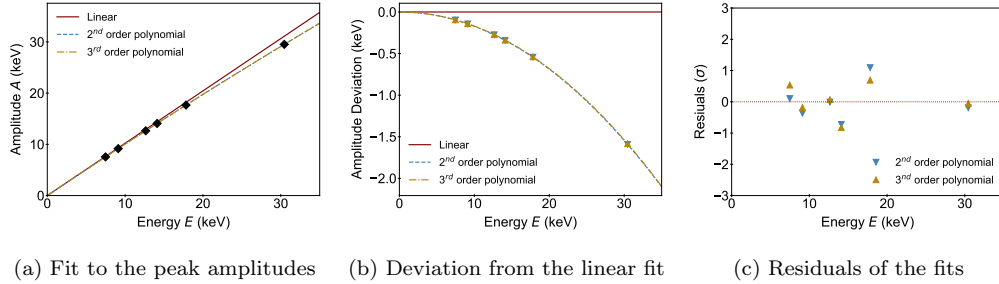


Figure 7: Calibration function for the measured  $^{83\text{m}}\text{Kr}$  spectrum: (a) fit to the peak amplitudes with a  $2^{\text{nd}}$  and  $3^{\text{rd}}$  order polynomial functions, with the linear component shown as well, (b) deviation from the linear fit, i.e., non-linearity, (c) residuals of the data points from the fit function, in the units of sigma of the found peak positions. Theoretical values for the peak energies taken from [21].

The measured spectrum stands as currently the highest resolution  $^{83\text{m}}\text{Kr}$  spectrum measured with a differential detector, to our present best knowledge, and will be discussed in more detail in the upcoming publications, after all the systematic effects, such as backscattering, have been fully investigated.

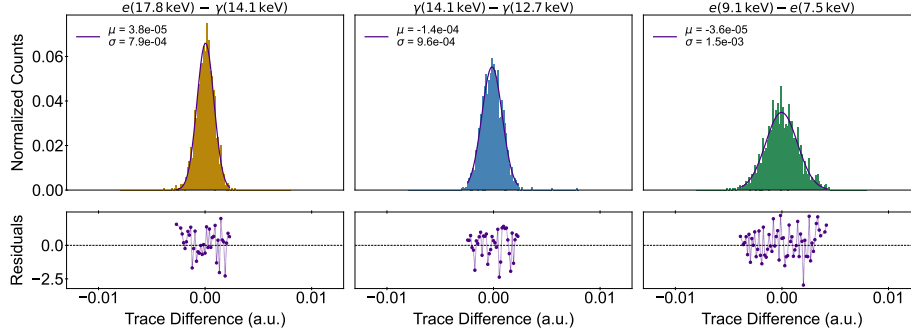
Looking towards the future, by building upon this work we plan to develop a quantum sensor demonstrator to further test and advance this technology for future experiments.

## Acknowledgments

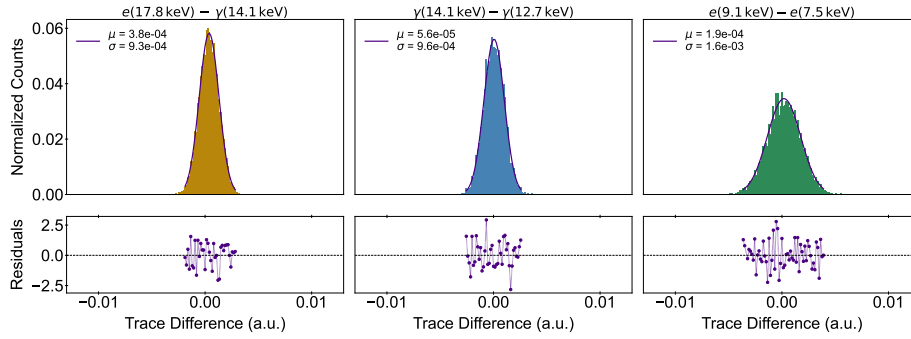
Funded by the Federal Ministry of Education and Research (BMBF) and the Baden-Württemberg Ministry of Science as part of the Excellence Strategy of the German Federal and State Governments. We further acknowledge support of the Helmholtz Association and, additionally, the Helmholtz Initiative and Networking Fund under grant agreement no. W2/W3-118. We thank Dr. Beate Bornschein from Tritium Laboratory Karlsruhe (TLK) for fruitful discussions.

## Appendix A. Appendix

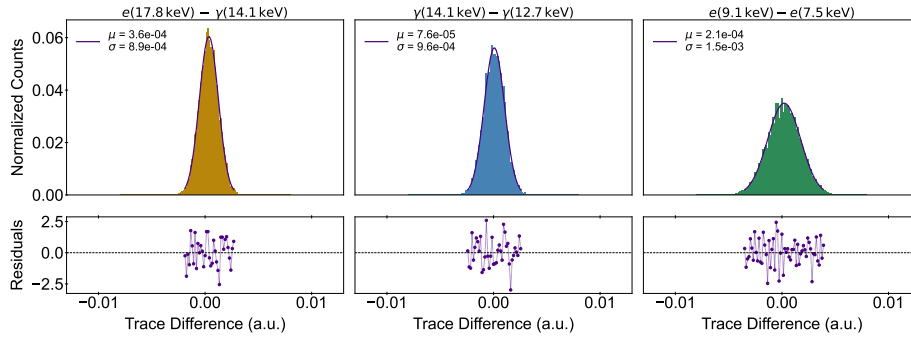
In order to confirm that the histograms of trace differences, shown in figure 5, are truly Gaussian, fit have been performed on individual histograms and are shown in figure A.8. As can be seen in the figure, all histograms are well described by a Gaussian function, and no visible strictures are present in the residuals. All fit results are summarized in table 2.



(a) Fits to histograms of signal differences taking into account 0.1 ms around the signal rise



(b) Fits to histograms of signal differences taking into account 0.5 ms around the signal rise



(c) Fits to histograms of signal differences taking into account 1.0 ms around the signal rise

Figure A.8: Fits to the histograms of the differences between individual signal traces, taking into account signal traces: (a) within the region of 0.1 ms around the signal rise, (a) within the region of 0.5 ms around the signal rise and (a) within the region of 1.0 ms around the signal rise, as shown in figure 5 (a). Each histogram is fitted with a Gaussian function, and fit results are reported in the legend. Residuals of the fit are shown below each respective histogram. Plots are shown in linear scale.

## References

- [1] Y. Fukuda, et al. (Super-Kamiokande), Evidence for oscillation of atmospheric neutrinos, *Physical Review Letters* 81 (1998) 1562–1567. URL: <https://link.aps.org/doi/10.1103/PhysRevLett.81.1562>. doi:10.1103/PhysRevLett.81.1562.
- [2] Q. R. Ahmad, et al. (SNO), Measurement of the Rate of  $\nu_e + d \rightarrow p + p + e^-$  Interactions Produced by  $^8B$  Solar Neutrinos at the Sudbury Neutrino Observatory, *Physical Review Letters* 87 (2001) 071301–. URL: <https://link.aps.org/doi/10.1103/PhysRevLett.87.071301>. doi:10.1103/PhysRevLett.87.071301.
- [3] J. Lesgourgues, S. Pastor, Neutrino cosmology and Planck, *New Journal of Physics* 16 (2014) 065002. URL: <https://dx.doi.org/10.1088/1367-2630/16/6/065002>. doi:10.1088/1367-2630/16/6/065002.
- [4] J. A. Formaggio, A. L. C. de Gouvêa, R. H. Robertson, Direct measurements of neutrino mass, *Physics Reports* 914 (2021) 1–54. URL: <https://www.sciencedirect.com/science/article/pii/S0370157321000636>. doi:<https://doi.org/10.1016/j.physrep.2021.02.002>, direct measurements of neutrino mass.
- [5] M. Kleesiek, J. Behrens, G. Drexlin, K. Eitel, M. Erhard, J. A. Formaggio, F. Glück, S. Groh, M. Hötzel, S. Mertens, A. W. P. Poon, C. Weinheimer, K. Valerius,  $\beta$ -Decay spectrum, response function and statistical model for neutrino mass measurements with the KATRIN experiment, *The European Physical Journal C* 79 (2019). URL: <http://dx.doi.org/10.1140/epjc/s10052-019-6686-7>. doi:10.1140/epjc/s10052-019-6686-7.
- [6] M. Aker, et al. (KATRIN), The design, construction, and commissioning of the KATRIN experiment, *Journal of Instrumentation* 16 (2021) T08015. URL: <https://dx.doi.org/10.1088/1748-0221/16/08/T08015>. doi:10.1088/1748-0221/16/08/T08015.
- [7] G. Beamson, H. Q. Porter, D. W. Turner, The collimating and magnifying properties of a superconducting field photoelectron spectrometer, *Journal of Physics E: Scientific Instruments* 13 (1980) 64. URL: <https://dx.doi.org/10.1088/0022-3735/13/1/018>. doi:10.1088/0022-3735/13/1/018.



- [8] V. M. Lobashev, et al., Neutrino rest mass and anomaly in the tritium  $\beta$  spectrum, *Nucl. Phys. A* 654 (1999) 982c–987c. doi:10.1016/S0375-9474(00)88585-1.
- [9] A. Picard, H. Backe, H. Barth, J. Bonn, B. Degen, T. Edling, R. Haid, A. Hermanni, P. Leiderer, T. Loeken, A. Molz, R. B. Moore, A. Osipowicz, E. W. Otten, M. Przyrembel, M. Schrader, M. Steininger, C. Weinheimer, A solenoid retarding spectrometer with high resolution and transmission for keV electrons, *Nuclear Instruments and Methods in Physics Research Section B: Beam Interactions with Materials and Atoms* 63 (1992) 345–358. URL: <https://www.sciencedirect.com/science/article/pii/0168583X9295119C>. doi:[https://doi.org/10.1016/0168-583X\(92\)95119-C](https://doi.org/10.1016/0168-583X(92)95119-C).
- [10] M. Aker, et al. (KATRIN), Direct neutrino-mass measurement based on 259 days of KATRIN data (2024). [arXiv:2406.13516](https://arxiv.org/abs/2406.13516).
- [11] F. Toschi, B. Maier, G. Heine, T. Ferber, S. Kempf, M. Klute, B. von Krosigk, Optimum filter-based analysis for the characterization of a high-resolution magnetic microcalorimeter, *Phys. Rev. D* 109 (2024) 043035. URL: <https://link.aps.org/doi/10.1103/PhysRevD.109.043035>. doi:10.1103/PhysRevD.109.043035.
- [12] M. Krantz, F. Toschi, B. Maier, G. Heine, C. Enss, S. Kempf, Magnetic microcalorimeter with paramagnetic temperature sensors and integrated dc-SQUID readout for high-resolution x-ray emission spectroscopy, *Applied Physics Letters* 124 (2024) 032601. doi:10.1063/5.0180903.
- [13] F. Mantegazzini, et al., Metallic magnetic calorimeter arrays for the first phase of the echo experiment, *Nuclear Instruments and Methods in Physics Research, Section A: Accelerators, Spectrometers, Detectors and Associated Equipment* 1030 (2022). doi:10.1016/j.nima.2022.166406.
- [14] S. Kempf, A. Fleischmann, L. Gastaldo, C. Enss, Physics and applications of metallic magnetic calorimeters, *J. Low Temp. Phys.* 193 (2018). doi:10.1007/s10909-018-1891-6.
- [15] A. Fleischmann, C. Enss, G. M. Seidel, *Metallic Magnetic Calorimeters*, Topics in Applied Physics, Springer, 2005, pp. 151–216. doi:10.1007/10933596\_4.

- [16] B. L. Zink, K. D. Irwin, G. C. Hilton, J. N. Ullom, D. P. Pappas, Erbium-doped gold sensor films for magnetic microcalorimeter x-ray detectors, *Journal of Applied Physics* 99 (2006) 08B303. doi:10.1063/1.2159207.
- [17] A. Burck, S. Kempf, S. Schäfer, H. Rotzinger, M. Rodrigues, T. Wolf, L. Gastaldo, A. Fleischmann, C. Enss, Microstructured magnetic calorimeter with meander-shaped pickup coil, *Journal of Low Temperature Physics* 151 (2008) 337–344. doi:10.1007/s10909-007-9659-4.
- [18] M. Müller, M. Rodrigues, J. Beyer, M. Loidl, S. Kempf, Magnetic microcalorimeters for primary activity standardization within the empir project prima-ltd, *Journal of Low Temperature Physics* 214 (2024) 263–271. doi:<https://doi.org/10.1007/s10909-024-03048-7>.
- [19] R. B. Firestone, V. S. Shirley, C. M. Baglin, S. Y. F. Chu, J. Zipkin, The 8th edition of the Table of Isotopes, Springer, Hungary, 1997. URL: [http://inis.iaea.org/search/search.aspx?orig\\_q=RN:29029102](http://inis.iaea.org/search/search.aspx?orig_q=RN:29029102).
- [20] M. Erhard, S. Bauer, A. Beglarian, T. Bergmann, J. Bonn, G. Drexlin, J. Goullon, S. Groh, F. Glück, M. Kleesiek, N. Haußmann, T. Höhn, K. Johnston, M. Kraus, J. Reich, O. Rest, M. Schlösser, M. Schupp, M. Slezák, M. Zbořil, High-voltage monitoring with a solenoid retarding spectrometer at the KATRIN experiment, *Journal of Instrumentation* 9 (2014) P06022. doi:10.1088/1748-0221/9/06/P06022.
- [21] D. Vénos, J. Sentkerestiová, O. Dragoun, M. Slezák, M. Ryšavý, A. Špalek, Properties of  $^{83\text{m}}\text{Kr}$  conversion electrons and their use in the KATRIN experiment, *Journal of Instrumentation* 13 (2018) T02012. URL: <https://dx.doi.org/10.1088/1748-0221/13/02/T02012>. doi:10.1088/1748-0221/13/02/T02012.
- [22] S. Schäfer, Entwicklung einer Detektorzeile aus metallischen magnetischen Kalorimetern zur hochauflösenden Röntgenspektroskopie an hochgeladenen Ionen, Ph.D. thesis, Kirchhoff-Institut für Physik, Universität Heidelberg, 2012.
- [23] K. M. Patel, S. Withington, A. G. Shard, D. J. Goldie, C. N. Thomas, Electron spectroscopy using transition-edge sensors, *Journal of Applied Physics* 135 (2024) 224504. URL: <https://doi.org/10.1063/5.0206487>. doi:10.1063/5.0206487. arXiv:2403.01160.